Available online at www.sciencedirect.com
SCIENCE DIRECT®
International Journal of Multiphase Flow 30 (2004) 1213–1234
International Journal of Multiphase Flow
www.elsevier.com/locate/ijmulflow

Experimental detection of bubble–bubble interactions in a wall-sliding bubble swarm

Atsuhide Kitagawa [a,*], Kazuyasu Sugiyama [b], Yuichi Murai [c]

[a] *Department of Mechanical and System Engineering, Kyoto Institute of Technology, Goshokaido-cho, Matsugasaki, Sakyou-ku, Kyoto 606-8585, Japan*
[b] *Center for Smart Control of Turbulence, National Maritime Research Institute, 6-38-1 Shinkawa, Mitaka, Tokyo 181-0004, Japan*
[c] *Division of Mechanical Science, Hokkaido University, Kita-ku, N13W8, Sapporo 060-8628, Japan*

Received 20 May 2003; received in revised form 1 July 2004

Abstract

Bubble–bubble interactions in a wall-sliding bubble swarm are investigated experimentally using a particle tracking velocimetry (PTV) technique. Firstly, the drag coefficient of a single wall-sliding bubble is measured, in which the distance between the wall and the bubble interface is much shorter than the average bubble diameter. Secondly, the probability distribution of the nearest bubble around individual bubbles in the bubble swarm is detected in the range from $Re = 1$ to around 20. Two kinds of statistical sampling techniques are used in order to identify the two-dimensional structure of the bubble–bubble interactions. A local modification of the drag coefficient in the swarm is obtained by calculating the interactive velocity of an individual bubble. Furthermore, the transition of a bubble's arrangement in the swarm is discussed by computing the relative velocity vector. The feature of the interaction patterns obtained by these techniques is classified based on Reynolds number.

Keywords: Bubble–bubble interaction; Bubbly flow; Wall-sliding bubble; Particle tracking velocimetry

* Corresponding author. Tel.: +81 75 724 7327; fax: +81 75 724 7300.
E-mail address: kitagawa@kit.ac.jp (A. Kitagawa).

0301-9322/$ - see front matter © 2004 Elsevier Ltd. All rights reserved.
doi:10.1016/j.ijmultiphaseflow.2004.07.002

1. Introduction

As the bubble number density increases in bubbly flows, the average bubble–bubble distance becomes so short that the behavior as a bubble swarm may be altered from that of a single bubble. The behavior of the bubble swarm depends primarily on the relative configuration of individual bubbles. It is generally expected that the relative bubble motion in a swarm is governed by bubble–bubble interactions. Such interactions are observed in the vicinity of the wall because of the high void fraction that is easily provided. Bubble interactions are recognized as a trigger of flow transition from bubbly flow to slug flow in two-phase pipe flows. Moreover, they are strongly related to the performance of many kinds of industrial techniques such as control techniques of the boundary layer using micro-bubbles, enhancement techniques of chemical reactions, and so on. From various perspectives, many investigations, both numerical and experimental, have been carried out on bubble interactions. Much of the interest has focused on the effect of the Reynolds number, Re, on bubble interactions because the interactions result from hydrodynamic forces among bubbles and these vary significantly with Re. This paper focuses on bubble–bubble interactions, which give not only the relative bubble motion but also the intrinsic bubble arrangement in the bubble swarm.

Previous theoretical analyses regarding bubble interactions led to the following conclusions. As low Re, the repulsive force acts horizontally on the bubble while the attractive force acts vertically. In contrast, in the potential flow, the attractive force acts horizontally on the bubble while the repulsive force acts vertically. Sangani and Didwania (1993) and Smereka (1993) carried out numerical simulations of the flow including a large number of massless spheres in the potential flow, and revealed that bubbles form a horizontally aligned cluster over time due to the horizontal attractive force. At moderate Reynolds numbers, Yuan and Prosperetti (1994) studied numerically the interaction of two spherical bubbles rising in tandem. They clarified that the vorticity diffusion from a leading bubble causes a drag modification of a trailing bubble and that dissipation function method cannot be applied to such a bubble–bubble interaction, even though $Re = 200$. Legendre and Magnaudet (1998) investigated numerically the interaction of two spherical bubbles rising side-by-side, and clarified that the sign of the lift coefficient changes in the range of $2.5 < Re < 25$. Using the front tracking method, Esmaeeli and Tryggvason (1998) carried out two- and three-dimensional numerical simulations of spherical bubbles rising at low Re. They demonstrated that the bubble configuration changes through the formation of a vertically oriented pair through a drafting event, and that a freely evolving array rises considerably faster than a regular array. In a similar numerical way, Bunner and Tryggvason (1999) performed three-dimensional numerical simulations of a flow field, including spherical bubbles and ellipsoidal bubbles. They focused particularly on bubbles rising with a nearly uniform distribution, revealing the difference between spherical bubbles and ellipsoidal bubbles due to vorticity generation and the interactions of deformable bubbles. Ruzicka (2000) proposed a mathematical model concerning the interaction of bubbles rising in line, comparing the results obtained by his model with previous results. Direct numerical simulations with respect to interactions between spheres subjected to a no-slip condition to its surface were performed by Kim et al. (1993) and Sugiyama et al. (2001).

On the experimental side, Stewart (1995) observed the interaction between several ellipsoidal bubbles accompanied by a deformation, estimating the relationship between bubble motion and bubble wake. Using scanning particle image velocimetry, Brucker (1998) measured the flow,

including ellipsoidal bubbles, and revealed the reconstruction of the bubble shape and the bubble wake structure. In order to compare the results with predictions of bubble interactions in potential flow, Zenit et al. (2001) researched experimentally the behaviors of a bubble suspension in a vertical channel at a high *Re* and a low *We*. In particular, they revealed the formation of horizontally oriented bubble clusters by analyzing results of image processing.

Despite the previous efforts, we still lack bubble interaction data for all angular directions. The purpose of the present study is to obtain experimentally a sufficient amount of basic data on two-dimensional bubble interactions in a bubble swarm rising along a nearly vertical solid wall. Such a wall-sliding bubble swarm is of great interest in applications: wall heat transfer in bubbly flows (e.g. Serizawa and Kataoka, 1988), ship drag reduction by micro-bubbles (e.g. Kodama et al., 2000) and electrode dynamics in hydrogen fuel cells (Nagai et al., 2003).

In the present study, the two-dimensional particle tracking velocimetry (PTV) technique is applied since the motion of a wall-sliding bubble swarm is completely two-dimensional. In fact, no bubbles overlap each other in the image projected from the perpendicular direction to the layer of the sliding bubbles. The topics reported in this paper are as follows: in the second section, experimental setup and methods are mentioned in detail. In the third section, the measurement of the drag coefficient of a single wall-sliding bubble is performed. In the fourth section, the measurement of the velocity vector of individual bubbles and the extraction of bubble–bubble interaction patterns in the wall-sliding bubble swarm are presented. Finally, the present study concludes with the features of bubble–bubble interactions classified by Reynolds number.

2. Experimental setup and methods

2.1. Single wall-sliding bubble measurement

Fig. 1 shows an outline of the experimental apparatus. The container made of a transparent acrylic resin, measures internally 1000 mm in height, 100 mm in width and 100 mm in depth. Silicone oil (Shinetsu, KF96) is filled up to a height of 850 mm into the container and the air bubble is injected in the vicinity of the wall from the bottom using a micro-syringe injector of which the outside and inside diameters are 0.47 and 0.13 mm, respectively. The bubble injection point is set at 3.0 mm from the wall. When many bubbles are simultaneously injected, convection due to their buoyancy near the wall is induced. Consequently, the bubble swarm approaches naturally close to the wall due to the lift force caused by the liquid velocity gradient. In contrast, when a small single bubble is injected, it does not always show a wall-sliding bubble. This is because the lift force acts on the bubble to leave the wall owing to a bubble deformation effect or an inertial effect at a small *Re* when the bubble moves parallel to the wall (Takemura et al., 2002). Therefore, the experimental tank is slightly inclined in order to force the bubble to slide on the wall. As a result, every bubble experiences sliding motion. The angle of the inclined wall is set at 4.5° to the vertical after confirming that an inclination of the bubble motion due to the lift force is approximately 2°–4° to the vertical in the range of all *Re* on which we focused. The lighting source is a halogen light and is set behind the test container through a translucent sheet. Each bubble is clearly projected as a hollow circular shadow by the back-lighting method. The visualized image is directly ported to a PC through a CCD camera system. The shutter speed of the camera is 1/1000 s and the frame rate

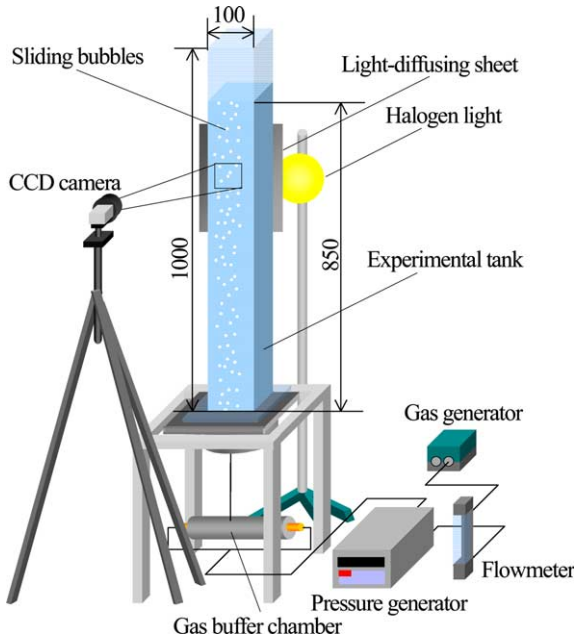

Fig. 1. Outline of experimental apparatus.

is 30 fps. The original images are digitized through an image capture board with a resolution of 1008×1018 pixels $\times$ 8 bit gray level. The measurement position in height is set at 650 mm from the bubble injection plane. The shooting area is 44.4 mm $\times$ 44.8 mm and the spatial resolution is 0.044 mm/pixel. Table 1 lists the experimental conditions. Here, ρ_L, ν_L and σ are the density, kinematic viscosity and surface tension coefficient, respectively. ρ_G is the gas density and R is the bubble radius. Reynolds number Re, Weber number We and Eötvös number Eo are defined as

$$Re = \frac{2VR}{\nu_L}, \qquad We = \frac{2\rho_L V^2 R}{\sigma}, \qquad Eo = \frac{4g(\rho_L - \rho_G)R^2}{\sigma}, \tag{1}$$

where V is the rise velocity of the single wall-sliding bubble and g is the gravitational acceleration.

Table 1
Experimental conditions

Liquid (silicone oil)				Gas ($\rho_G = 1.2$ kg/m^3)			
	ρ_L (kg/m^3)	ν_L (m^2/s)	σ (N/m)	R (mm)	Re (−)	We (−)	Eo (−)
Case a1	977	125.9×10^{-6}	20.9×10^{-3}	0.73–1.15	0.1–0.4	0.01–0.1	1.0–2.4
Case a2	972	62.9×10^{-6}	20.8×10^{-3}	0.77–1.10	0.5–1.6	0.03–0.2	1.1–2.2
Case a3	965	38.2×10^{-6}	20.8×10^{-3}	0.67–1.06	0.7–3.4	0.03–0.4	0.8–2.1
Case a4	943	12.3×10^{-6}	20.1×10^{-3}	0.52–0.91	3.1–16	0.1–1.0	0.5–1.5

2.2. Wall-sliding bubble swarm measurement

For wall-sliding bubble swarm measurement, nearly the same experimental apparatus and illumination methods are used, as mentioned in Section 2.1. The gas flow rate is controlled using a volumetric type tube pump (Inai CTP-1). Air bubbles are periodically injected through capillary needles of which the inside diameter is 0.5 mm. The bubble injection point is same as in Section 2.1. Incidentally, the wall-sliding bubbles are naturally generated without an inclination in the container because of the liquid convection induced by the rising bubbles. Thereby, the position of bubble injection at the bottom does not significantly affect the structure of the sliding bubbles. In order to accurately compare this situation with the single sliding bubble, however, the container is intentionally inclined at an angle of 4.5°. Table 2 shows the experimental conditions. The bubble radius R, Reynolds number Re, Weber number We and Eötvös number Eo in Table 2 are the mean values averaged over all of the bubbles. S is the ratio of the standard deviation of the bubble radius to the mean bubble radius. In which, S is less than 1.3% in any case so that the bubble–bubble interaction is detected approximately as a mono-dispersed system. The Reynolds number is defined not by the mean bubble rise velocity relative to the mean liquid velocity but the mean bubble rise velocity relative to the wall. This is a reasonable representation of the Reynolds number because the wall-sliding bubble is affected mainly by the solid wall rather than the motion relative to the liquid.

A suitable range of gas flow rates is chosen in order to have enough interacting but not coalescing bubbles in the swarm. The gas flow rates for cases b1 to b3 are 20, 5 and 2.5 ml/min, respectively.

2.3. Measurement technique

The procedures associated with the PTV technique for the wall-sliding bubbles are as follows (Fig. 2(a)–(d) show the images of the bubbles corresponding to each procedure):

1. The brightness of the original images is inverted for easy handling of the process below.
2. The edges of the bubbles are emphasized using Prewitt's operator (1970). This operator has some advantages: the effect of the noise for the images is smaller than other differential operators and the slight difference in the brightness near the bubble interface is captured quite well.
3. The images are binarized using the method proposed by Otsu (1979) and the centroids of the bubbles are then calculated from the binarized image.

Table 2
Experimental conditions

Liquid (silicone oil)				Gas ($\rho_G = 1.2$ kg/m^3)				
	ρ_L (kg/m^3)	ν_L (m^2/s)	σ (N/m)	R (mm)	S (%)	Re (–)	We (–)	Eo (–)
Case b1	972	62.9×10^{-6}	20.8×10^{-3}	1.00	1.21	1.3	0.2	1.9
Case b2	965	38.2×10^{-6}	20.8×10^{-3}	0.96	0.48	2.8	0.3	1.7
Case b3	943	12.3×10^{-6}	20.1×10^{-3}	0.86	0.93	15	1.0	1.4

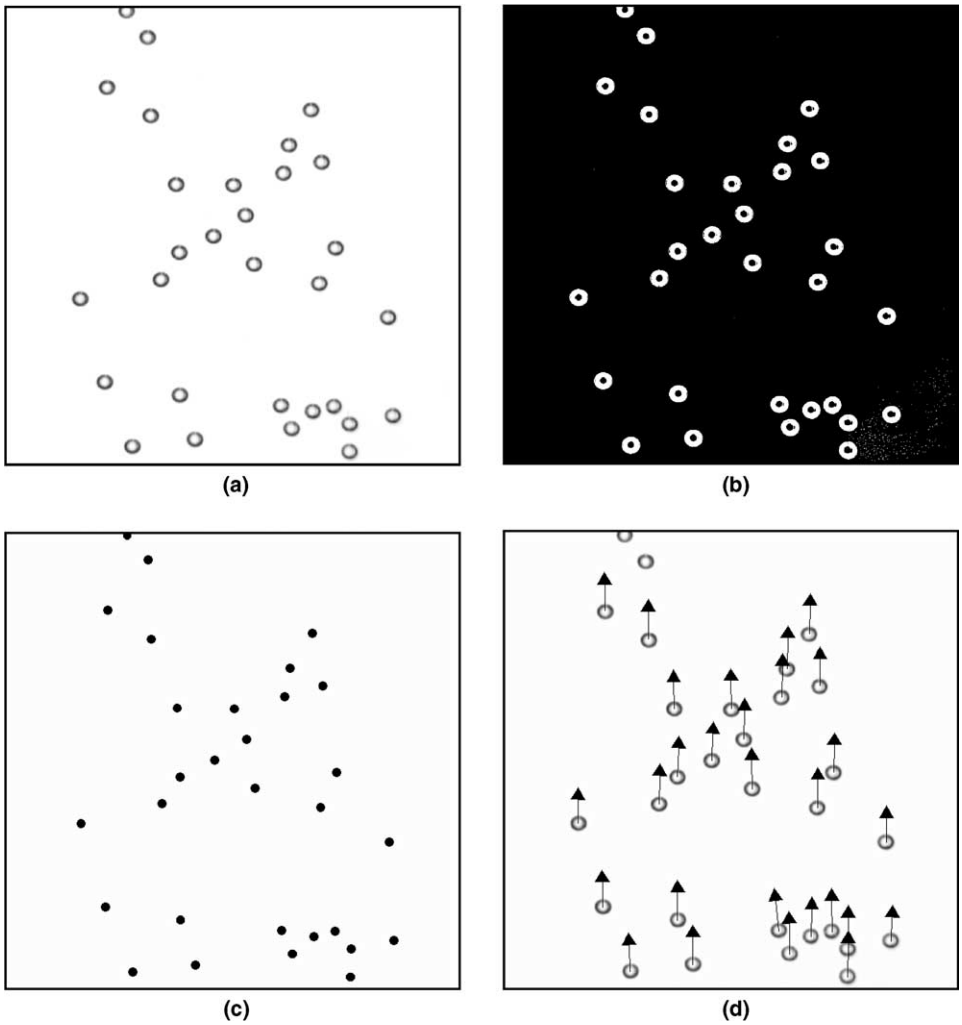

Fig. 2. Images used at the each phase of the image processing: (a) original image; (b) image at steps 1 and 2; (c) image at step 3; (d) image at step 4.

4. The velocity vectors of the bubbles are calculated by the three-time-step tracking method with a time separation of 1/30 s between image pairs. In the three-time-step tracking method, the position of the bubble in the third frame is searched for from linear extrapolation with the bubble velocity vector which was measured at the former step.

2.4. Evaluation of image measurement accuracy

To measure accurately the slight fluctuations in the velocity of the bubbles induced by the bubble–bubble interaction, it is necessary to obtain the centroid of the bubble (procedure (3)) with high efficiently and to completely remove the miss-pairing among the three frames (procedure

(4)). Therefore, performance evaluation for the binary labeling method and the three-time-step tracking method are carried out using a set of the test images.

Fig. 3 shows the comparison of results with two kinds of popular PTV algorithms. N_B is the total bubble number in the image, D_B is the ratio of the detected bubble number to the total bubble number in the image and I_B is the ratio of the number of incorrect vectors to that of the correct vectors, respectively. Each value is averaged over 30 cases provided with random number series. BICC is the binary image cross-correlation method (e.g. Yamamoto et al., 1996) which works well for the densely arranged dispersions. It is based on the spatial correlation of the bubble arrangement between two consecutive images. 4-PTV is the four-time-step tracking method (e.g. Nishino et al., 1989), which works, well for large displacements in relatively dilute dispersion. It is based on the temporal continuity of the bubble's motion. It is confirmed from Fig. 3 that the D_B of the present algorithm 3-PTV keeps over 90% and I_B lies entirely at 0% for any value of N_B. This superiority to the other two algorithms allows us to measure the motion of the bubble swarm with high reliability. Note that bubbles near the upper region in the image cannot be detected because such bubbles have no centroids in the second frame. Hence, around 10% of the bubbles' data will vanish in the 3-PTV and BICC algorithm, and 20–30% of the data vanishing occur in the case of 4-PTV. The reason for the increase in I_B in 4-PTV is explained simply by the fact that every bubble

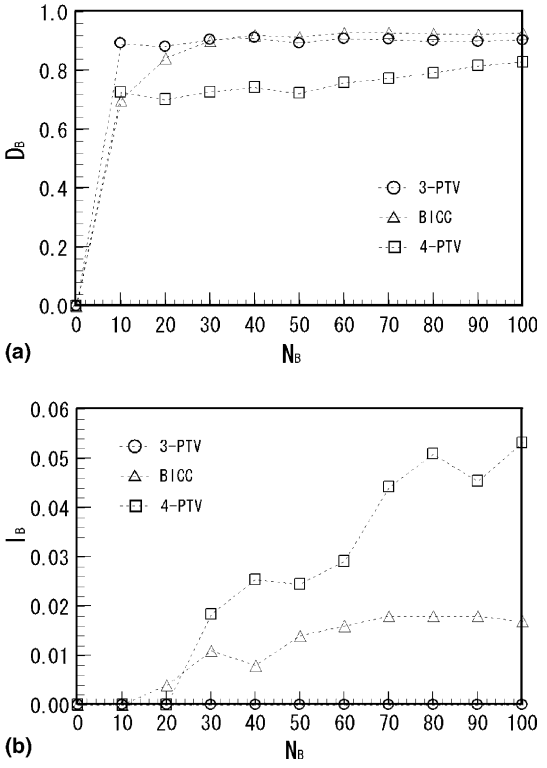

Fig. 3. Performance evaluation for three-time-step tracking method: (a) ratio of detected bubble; (b) ratio of incorrect velocity.

has a similar rising motion. That of BICC is explained by the occurrence of a sudden lack of spatial correlation during the interaction among closed bubbles.

The measurement uncertainty of the PTV technique in the present study is estimated as follows. The constituent pixel number of each bubble ranges from 600 to 2200 pixels. The displacement of the centroids of the bubble is 30–100 pixels per frame. The distance between the CCD camera and the bubble is approximately 250 mm and the error for the displacement of the centroid of the bubble is a maximum of 0.158 mm because of the effect of the viewing angle to the shooting area. Consequently, it is estimated that the measurement accuracy of the velocity vector and the relative error with respect to the rising bubble velocity are within 4.55 mm/s and 4.3%, respectively. The bubble diameter is calculated from the equivalent area of the constituent pixels. The drag coefficient of the bubble is calculated from substituting the bubble diameter and the bubble velocity into the balance equation between the buoyancy and the drag. The effect of the inclination of the tank for calculating these forces is taken into account using the tangential component of the gravitational acceleration to the wall. The uncertainty in the drag coefficient is therefore approximately 5.9%.

3. Measurement of a single wall-sliding bubble

To extract the effect of bubble–bubble interactions in wall-sliding bubble swarms, the drag coefficient of a single wall-sliding bubble must be measured as a function of *Re*. Takemura et al. (2002) experimentally measured the drag coefficient of a rising bubble in the vicinity of a wall. Their results were limited to the case where the minimum distance between the bubble interface and the wall was longer than the bubble radius. In contrast, in the present study, the maximum distance between the bubble interface and the wall is less than 5% of the bubble diameter. Therefore the drag coefficient cannot simply be predicted by extrapolating their experimental results. On the other hand, the motions of solid spheres in the vicinity of the wall are theoretically well understood. As representative theoretical studies, O'Neill (1964) derived the drag force acting on a rigid particle slowly moving in a direction parallel to the wall. However, the problem of the drag coefficient of the bubble near the wall has yet to be completely solved, to our knowledge. For this reason, the drag coefficient of a single wall-sliding bubble is measured.

Fig. 5 shows the drag coefficient of a single wall-sliding bubble as a function of Reynolds number. The effects of contamination in the liquid with respect to the drag coefficient are negligible since silicone oil with stable physico-electrical properties at the gas–liquid interface is used. The measurement data are compared with the following correlation for the drag coefficient of a bubble in infinite liquid, which was proposed by Mei et al. (1994):

$$C_{\mathrm{DC}} = \frac{16}{Re}\left[1 + \left\{\frac{8}{Re} + \frac{1}{2}\left(1 + \frac{3.315}{\sqrt{Re}}\right)\right\}^{-1}\right]. \tag{2}$$

It is known that at low *Re*, Eq. (2) is in agreement with the asymptotic solution proposed by Taylor and Acrivos (1964) while at high *Re*, it is in agreement with the boundary-layer solution proposed by Moore (1963).

Fig. 4 shows the relationship between the drag coefficient and the Reynolds number of a single wall-sliding bubble. The figures (a)–(d) are the data obtained for different silicone oils resulting in different kinematic viscosities. The hollow circles stand for the measurement data of single wall-sliding bubbles. The solid curves stand for the drag coefficient of single free-rising bubbles in infinite liquid calculated using Eq. (2). The solid circles in Fig. 4(c) represent measurement data points of a single free-rising bubble in our experimental system. It is confirmed that accurate measurements are successfully achieved in the present study. For the measurement results overall, it is found that the difference in the drag coefficient between the wall-sliding bubble and the free-rising single bubble (shown by the solid curves) expands with decreasing *Re*. This fact indicates simply that the effect of the wall appears at low *Re* since the momentum transfer due to viscosity occurs across a wide area around the bubble interface in those cases. However, it cannot be ignored that the distance between the bubble interface and the wall also varies with changing bubble size and viscosity of the liquid. In fact, the distance is governed by the lift force in all of the cases. The effect of the lift force induced by a solid wall has recently been analyzed by Takemura et al. (2002). They reached the conclusion that the ratio of the buoyancy to lift force becomes large for lower Reynolds numbers. This tendency may also explain the results of our measurement data though the ratio of the distance to the bubble radius is much shorter in our case than in their

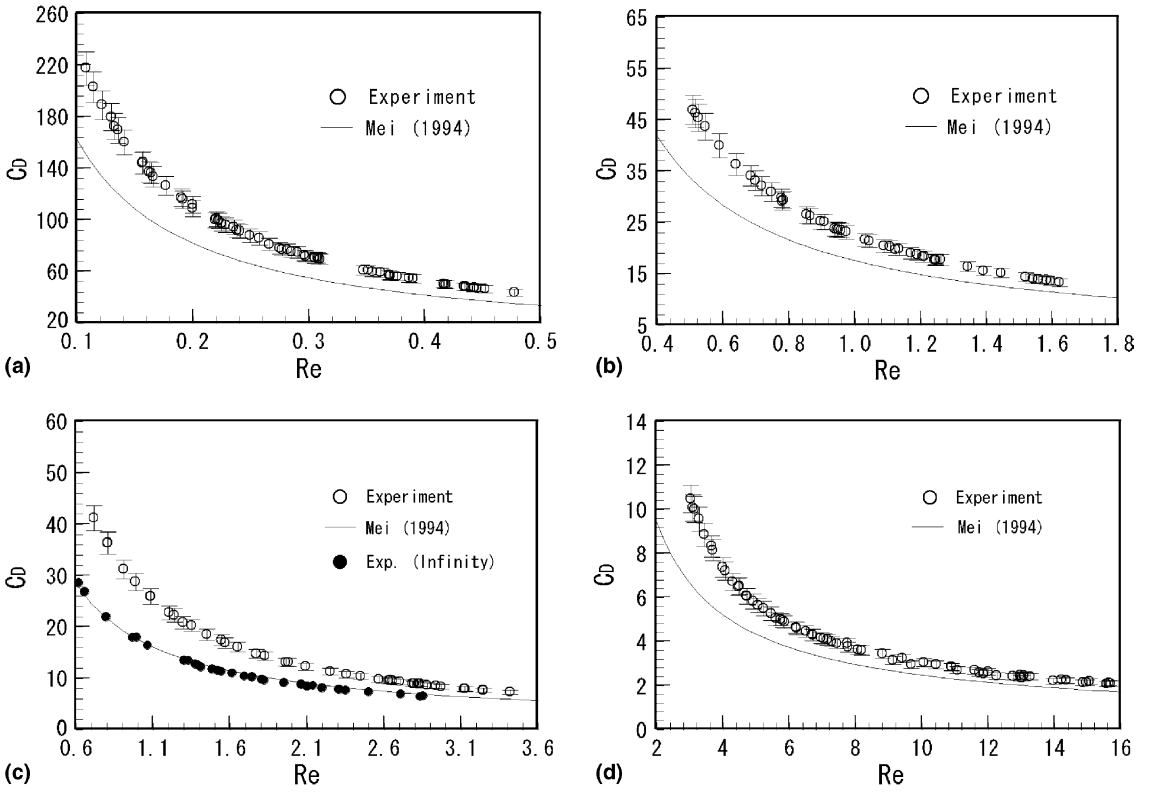

Fig. 4. Drag coefficient of single wall-sliding bubble as a function of Reynolds number: (a) case a1; (b) case a2; (c) case a3; (d) case a4.

analysis. Unfortunately, the distance cannot be measured directly because the width of defocused bubble interface on the image plane is almost similar to the distance. Therefore, the data presented here on drag coefficient is only referential and can be evaluated relative to the free-rising single bubble value in an infinite liquid. However, at least, it can be said that all of the data on the drag coefficient have continuous curves with respect to Reynolds number for any kind of silicone oil. This feature is sufficient to allow the bubble–bubble interaction component to be extracted, which is obtained by subtracting the motion component of the single bubble from direct measurement data of the bubble swarm.

A more detailed discussion on the present data is made as follows: when Reynolds number increases, the drag coefficient of a wall-sliding bubble reaches almost the same value as that of a free-rising bubble calculated with Eq. (2). The difference between the two at $Re = 15$ is around 15% relative to the absolute value. Of course, this feature cannot be explained simply by the reduction in the vorticity diffusion between the bubble interface and the wall surface. The slight deformation of the high Reynolds number bubble must be taken into account since the Weber number of the case a4 (see Table 1) gets almost 1.0. In such a case, the deformation of the bubble interface makes the bubble produce additional lift force and hence, the bubbles will actively leave the wall to have the characteristics of a free-rising bubble. In contrast, the maximum difference is around 30% at the lowest Reynolds number of $Re = 0.1$ where the rise velocity is reduced by 30% as a result of the wall effect.

4. Measurement of the wall-sliding bubble swarm

4.1. Macroscopic features of average bubble rise velocity in the bubble swarm

Before discussing the bubble–bubble interaction, the relationship between the bubble rise velocity and the void fraction is evaluated in order to grasp the macroscopic features of the bubble swarm. For free-rising bubbles or free-settling particles, the relationship between the terminal velocity and the volume fraction of the dispersion have been investigated experimentally (e.g. Zuber, 1964), theoretically (e.g. Sangani et al., 1991) and numerically (e.g. Esmaeeli and Tryggvason, 1998; Sugiyama et al., 2001). As a suitable representation of the void fraction for the wall-sliding bubbles, the bubble shadow area fraction is employed instead of the bubble volume fraction since the wall-sliding bubbles do not distribute in the spanwise direction. It equals to the ratio of total projected area of bubbles to the measurement area, i.e., a kind of two-dimensional void fraction defined with dimension of area.

Fig. 5 shows the relationship between the shadow area fraction A_S and the Reynolds number ratio Re_S/Re_0. The former is defined as

$$A_S = \sum_{i=1}^{N_B} \pi R_i^2 / L_x L_y, \tag{3}$$

where L_x and L_y are the lengths of the shooting area in the horizontal and vertical directions, respectively. The numerator represents the total projected area of the bubbles. Re_S and Re_0, shown in Fig. 5, are the average Reynolds numbers of the bubble swarm and of the single

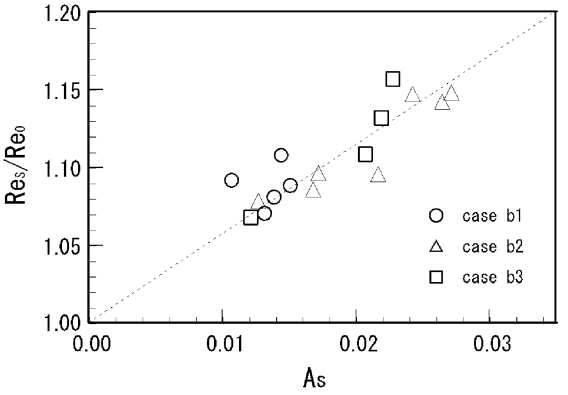

Fig. 5. Relationship between the shadow area fraction of sliding bubble and Reynolds number ratio.

wall-sliding bubble, respectively. The value of Re_0 is given by interpolating the measurement results shown in Section 3 and is not a function of A_S. From Fig. 5, it is confirmed that Re_S/Re_0 in all cases increases approximately linearly with A_S. The gradient is around 6 in the present measurement range, which is relatively large in comparison with the gradient of average density reduction due to increase of bubbles. This results from mainly two effects. One is the increase of the mean liquid velocity in the vicinity of the wall due to buoyancy effect of wall-sliding bubbles. Another one is a reduction in the drag acting on individual bubbles in a swarm as the bubble concentration increases. Furthermore, the gradient of Re_S/Re_0 with respect to A_S is not dependent so much on the liquid viscosity (see the difference among the three cases). In the range of the present Reynolds numbers and gas flow rates, therefore, the modification of the bubble rise velocity is roughly governed by the bubble shadow fraction. This is similar in terms of physics to the free-rising bubbles or free-settling particles in unbounded space where the average rise or settling velocity was approximately expressed as a function of the void fraction in 3-D space (e.g. Zuber, 1964; Sugiyama et al., 2001). After understanding this global feature, the local two-dimensional structure of the bubble swarm is to be analyzed below.

4.2. Sampling technique of bubble–bubble interaction patterns

Fig. 6 shows samples of the original images with the velocity vectors of bubbles obtained for $R = 1.19$ mm at two positions. The average Reynolds number here is 47. At the lower position (Fig. 6(a)), the bubbles maintain the homogenous arrangement which is provided by the nozzle arrangement interval and the bubble generation period. The homogenous distribution is collapsed and changes to an inhomogeneous one in the upper region (Fig. 6(b)). No clear difference is identified in the bubble behavior at the upper position when subjected to a weak dynamic disturbance in the bubble injection needle. This implies experimentally that the initially uniform distribution is unstable and that there exists a local two-dimensional bubble–bubble interaction causing a transition in the distribution. According to our analysis with a bubble probability distribution, at the lower position bubbles have a tendency to be oriented vertically because of the drafting event while at the upper position bubbles are preferentially oriented horizontally. A similar investigation was numerically performed by Esmaeeli and Tryggvason (1998) for the free-rising bubbles,

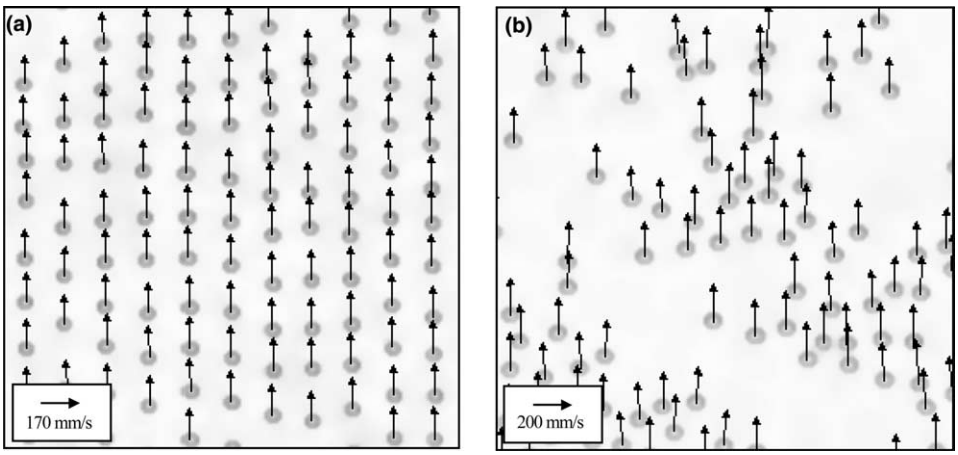

Fig. 6. Experimental images and bubble velocity vectors for $R = 1.19$ mm at $Re = 47$: (a) $Y = 250$ mm $\pm$ 25 mm; (b) $Y = 650$ mm $\pm$ 25 mm.

in which a weighted average of the pair distribution function, so called 'asymmetry index' was employed to determine the bubble distribution pattern; note however that this index is calculated over several bubbles in a certain finite domain while in the present study the relation between two bubbles which are the nearest with respect to each other are focused, as mentioned later. Although the statistical method and flow configurations in each study are different, the present experimental result is qualitatively in agreement with their numerical simulation result. In addition, the velocity vector of individual bubbles has a mainly vertical upward velocity component at the lower position while the horizontal one appears at the upper position. The magnitude of the horizontal velocity is approximately 10% of the vertical one in the maximum.

The technique of detecting this velocity component is as follows:

1. The nearest bubble to the one focused on is chosen. For instance, when the bubble n_i in Fig. 7 is chosen as the focused bubble, the bubble n_j corresponds to the nearest bubble. The relative position vector of the nearest bubble to the focused bubble is then calculated, i.e., $x = X_j - X_i$, $y = Y_j - Y_i$. Only the pairs for which the two bubbles are the nearest are counted in the statistical analysis later.
2. The differential velocity vector between the focused bubble and the nearest bubble is calculated, i.e., $\mathbf{u}_R = \mathbf{u}_j - \mathbf{u}_i$, which is called the 'relative bubble velocity vector' in the present study. This quantity is a measure of the relative motion of the two closed bubbles. Note that the relative bubble velocity also appears in the case where the two bubbles have different radii. Thus, only the pair having the relative deviation within $\pm 2.0\%$ to the mean bubble radius is counted for the statistics.
3. The differential velocity vectors between the nearest bubble and the distant bubble is calculated, i.e., $\mathbf{u}_I = \mathbf{u}_j - \mathbf{u}_\infty$. This is named the 'interactive bubble velocity vector' in the present study. Here, $\mathbf{u}_\infty$ is defined by the velocity vector of the bubble which is not affected by any other bubble. It is equivalent to the velocity of a single bubble, as measured in Section 3.

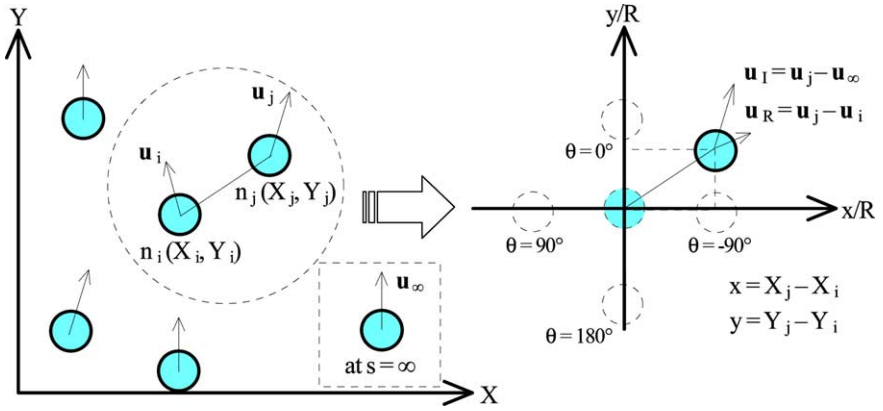

Fig. 7. Sampling technique of bubble–bubble interaction patterns.

4. The relative bubble velocity vector and the interactive bubble velocity vector for all of the relative position vectors are averaged using a sufficient number of sampled bubble pairs.

This procedure is repeated for each frame. For the reliability of the averaged map, more than 20,000 bubble pairs are used in each of the experimental conditions.

It is important to note that the aim of the above-mentioned technique is to extract the statistical two-bubble interaction in the bubble swarm. The data obtained will be slightly different from that of pure two-bubble interactions though similar phenomena are actually identified.

4.3. Probability distribution of nearest bubble in the bubble swarm

Fig. 8 shows the probability distribution of the nearest bubble around each of the bubbles in an equilibrium state, i.e., the upper position. The probability of the occurrence of a nearest bubble is defined as $N/N_{\max}$, where N and $N_{\max}$ are the numbers of the nearest bubbles counted in each grid and the maximum number of nearest bubbles in all of the area, respectively. The gray-scale in the figure is proportional to the probability. The grid division number is 28 in both the radial and circumferential directions in the detection radius, $8R$. There are few occurrences inside the radius of $3R$ since the sampled number of the nearest bubble is quite small. The probability distribution is determined from the results of the bubble–bubble interactions. It simultaneously indicates the region where the bubble–bubble interaction takes place. From the result, the following points have been established. (1) In Fig. 8(a) and (b), the nearest bubbles distribute significantly in the vertical direction. The peak value is in the range of about $|x/R| = 2$ and $|y/R| < 5$–6 for $Re = 1.3$, and $|x/R| = 1$ and $|y/R| < 4.5$–6 for $Re = 2.8$. This implies that the bubbles tend to rise in the vertical in-line arrangement for low Reynolds numbers. (2) In contrast, for high Reynolds numbers, it can be seen from Fig. 8(c) that the nearest bubbles distribute in the horizontal direction. This fact tells us that the bubbles under these conditions result in horizontally laid clusters. It is known that potential flow analysis leads to the same result. However, the phenomenon here is essentially different because of the invalidity of the inviscid approximation at $Re = 15$.

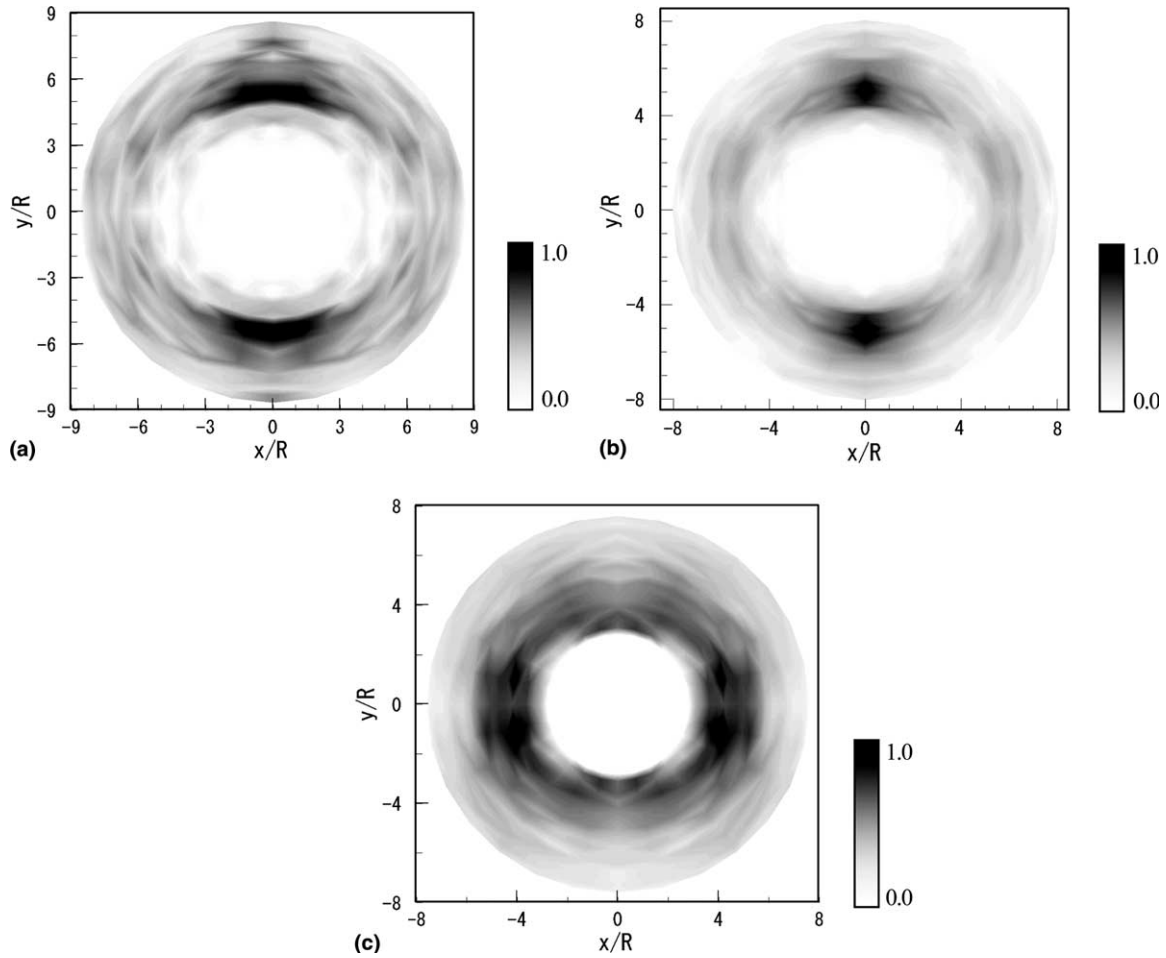

Fig. 8. Probability distribution of the nearest bubbles: (a) case b1; (b) case b2; (c) case b3.

4.4. Bubble–bubble interactions identified by the interactive bubble velocity vector field

Fig. 9 shows the grid-averaged results of the interactive bubble velocity vectors $\mathbf{u}_I$ for the three cases. The grid system is the same as in Fig. 8. The horizontal and vertical components of $\mathbf{u}_I$ increase as the bubble–bubble distance decreases, and its magnitude varies with Reynolds number. From this result it can be concluded that the bubble–bubble interaction depends on the bubble–bubble distance, bubble–bubble angle and Reynolds number. Therefore, an accurate model of the bubble–bubble interaction cannot be determined if the effect of one of those parameters is poorly understood. All of the cases of bubbles at diagonal upper positions relative to a focused bubble have faster horizontal velocity components of $\mathbf{u}_I$ as bubbles close to each other. This results from the liquid flow induced around the lower bubble, which is generated in a similar way to a doublet to push the upper bubble. The length of the arrows shown in the figures is normalized by the rise velocity of a single bubble in each case. The relative component of the interactive velocity is larger for small Reynolds numbers.

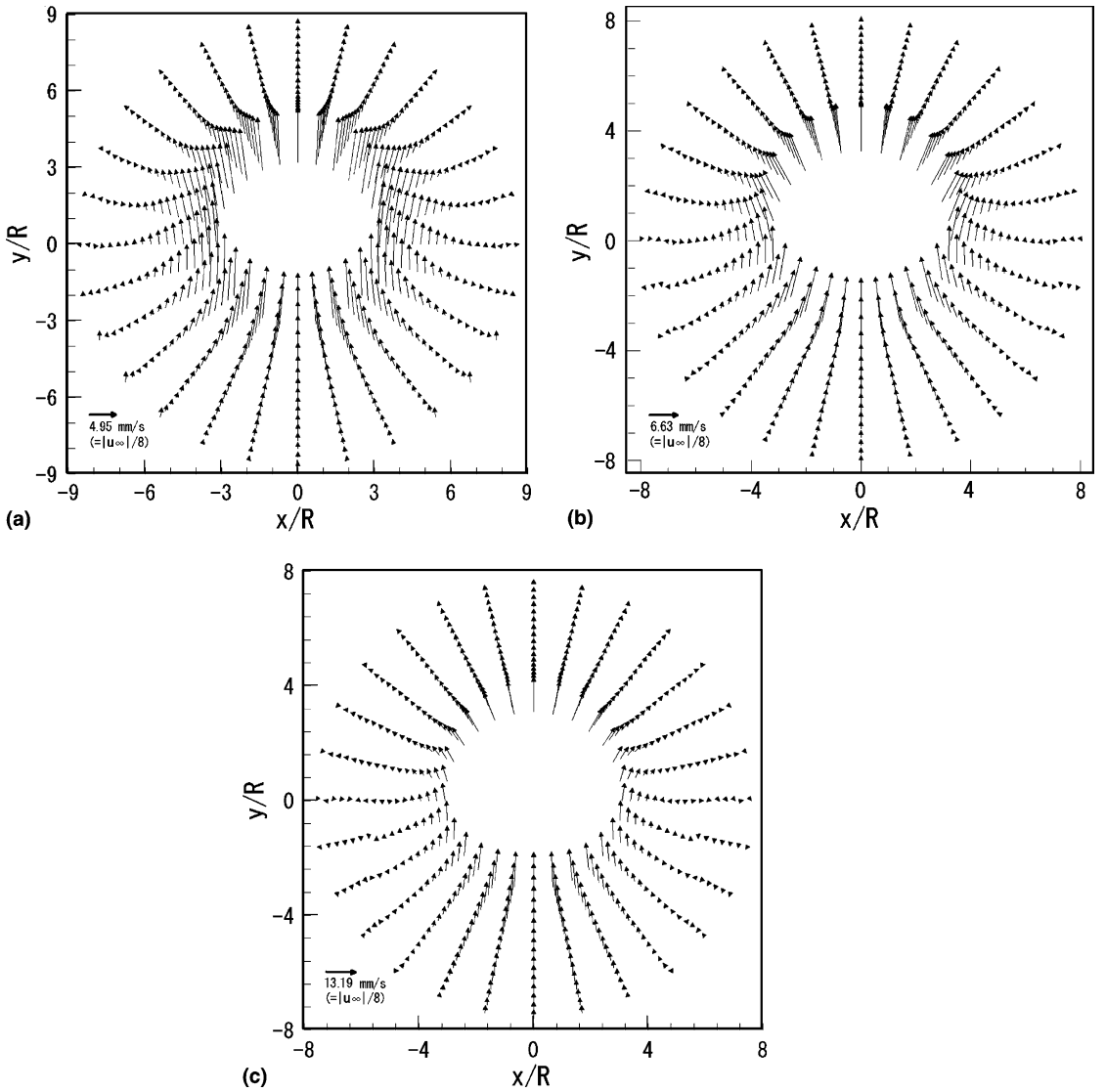

Fig. 9. Distribution of the interactive bubble velocity vectors: (a) case b1; (b) case b2; (c) case b3.

In order to discuss these two-dimensional characteristics in detail, the relationship between the position and the interactive bubble velocity components in the four orientations is picked up, as shown in Fig. 10. Here, the right side figures show the vertical component of the interactive bubble velocity v_I, while the left side figures show the horizontal component u_I. Both values are normalized by the rise velocity of a single bubble. The axis s is defined by the distance between the centroid of the two bubbles normalized by the bubble radius R, i.e., $s = (x^2 + y^2)^{1/2}/R$. The definition of θ is shown in Fig. 7. The following points are discussed with this figure:

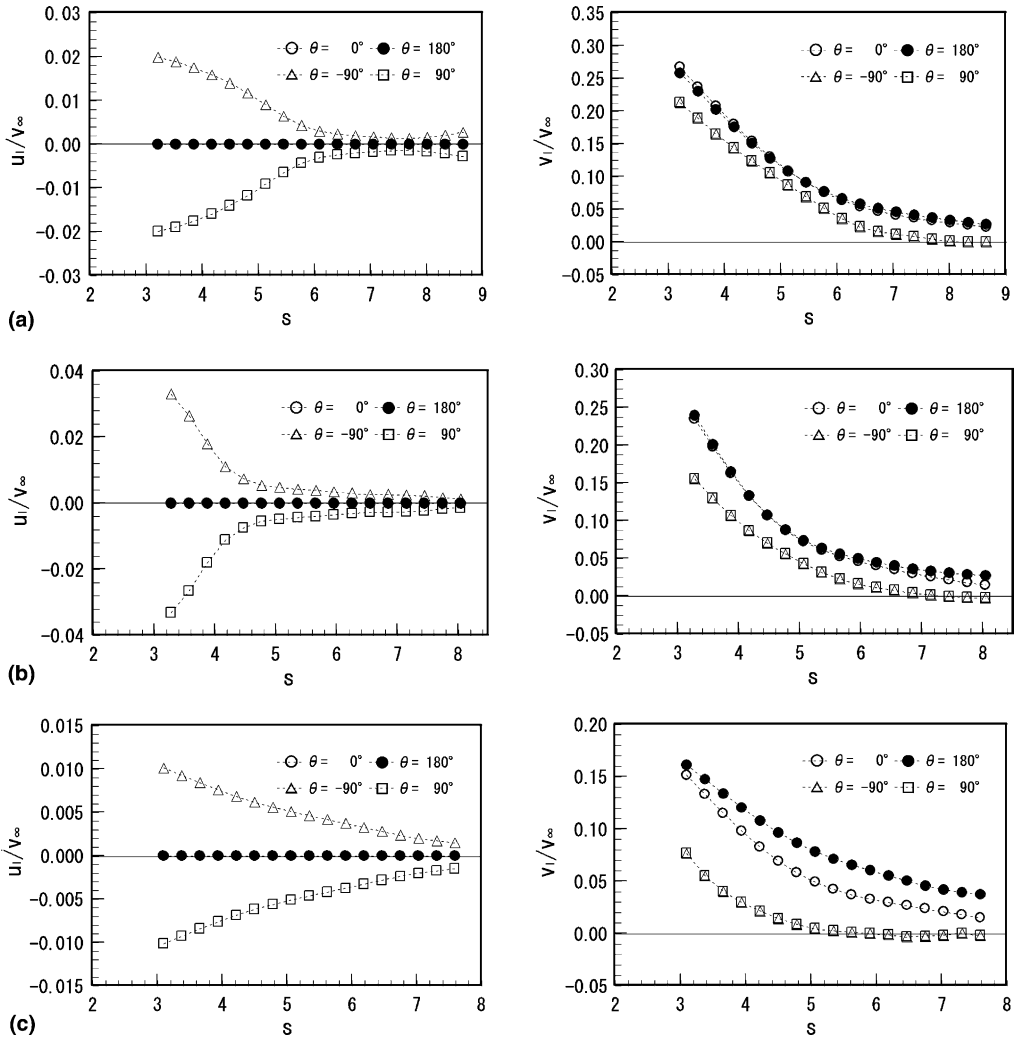

Fig. 10. Interactive bubble velocity in four orientations. The right sides show the vertical interactive bubble velocity while the left sides show the horizontal one: (a) case b1; (b) case b2; (c) case b3.

1. For all of the cases, the rise velocities of the bubbles at $\theta = 0°$ and 180° are higher than those of other directions (see the figures on the right side). That is, the interaction mainly occurs in the bubble's rising direction while the horizontal interaction is induced rather slowly.
2. For all of the cases, the horizontal velocity component that forces bubbles repulsing each other is induced when two bubbles rise at $\theta = 90°$ and/or $-90°$. Assuming a phenomenological similarity to two-bubble interactions in unbounded space, the reason for this can be explained by the numerical study of Legendre and Magnaudet (1998). That is, in situations of low Reynolds numbers, the vorticity diffusion from the bubble interface causes the liquid velocity between the bubbles to reduce. As a consequence, the pressure and the normal shear stress there become high and hence the repulsive force is induced.

3. For all of the cases, bubbles rising side-by-side also have higher rise velocities than single bubbles (see the data for $\theta = 90°$ and $-90°$). This means that the drag is reduced as the two bubbles rise close to one another.
4. In the cases b1 and b2 with low Reynolds numbers, the rise velocities of bubbles at $\theta = 0°$ are similar to those of bubbles at $\theta = 180°$ (see Fig. 10(a) and (b)). In contrast, in the case b3 with a high Reynolds number, the rise velocity of the bubbles at $\theta = 180°$ is higher than those of bubbles $\theta = 0°$ over a wide range of distances (see Fig. 10(c)). The effect of the interaction remains, even though the distance s reaches around 8. This indicates that the wake of the upper bubble induces a long entrainment in the downstream.

4.5. Drag modification of individual bubble in the bubble swarm

Fig. 11 shows the ratio of the drag coefficient of the nearest bubble C_D to that of the distant bubble $C_{D\infty}$, which corresponds to $|\mathbf{u}_\infty|^2/(v_I + |\mathbf{u}_\infty|)^2$. The drag coefficient is calculated from the vertical component of the absolute bubble velocity, i.e., bubble rise velocity. The gray level is drawn proportional to the reduction ratio of the drag coefficient. The results are as follows: (1) the drag coefficient ratios for cases b1 and b2 isotropically reduce in all of the angular directions as the bubble–bubble distance decreases (see Fig. 11(a) and (b)). This is because the effect of isotropic velocity diffusion due to the viscosity is dominant at low Reynolds numbers. (2) In contrast, for the case b3 with the high Reynolds number, the drag coefficient ratio anisotropically reduces in the vertical direction (see Fig. 11(c)). This results from the increase in the entrainment effect of the focused bubble.

Fig. 12 shows the drag coefficient ratio for $\theta = 90°$ and $180°$ as a function of Reynolds number. It is shown that $C_D/C_{D\infty}$ for all the cases reduces as the bubble–bubble distance s decreases. The reduction in magnitude of $C_D/C_{D\infty}$ for the tandem arrangement $\theta = 180°$ is 30% in the maximum, and is larger than that for the side-by-side arrangement $\theta = 90°$, by the same reason mentioned before. Simultaneously, the reduction in magnitude decreases with increasing Reynolds number. The measurement result confirms that the smaller the Reynolds number, the more the flow fields around individual bubbles are altered by the other bubble's approach. Similar characteristics were demonstrated in a numerical way by Yuan and Prosperetti (1994) and Legendre and Magnaudet (1998) for an infinite liquid.

4.6. Bubble–bubble interaction explained by the relative bubble velocity vector field

In this section, the bubble–bubble interaction is discussed with the results of the relative bubble velocity vector. The relative bubble velocity vector explains directly the relative motion of bubbles inside the swarm so that the attractive and repulsive behaviors of the two closed bubbles can be clarified.

Fig. 13 shows the grid-averaged results of the relative bubble velocity vectors $\mathbf{u}_R$. The lengths of the segments drawn in the figure are normalized by the absolute rise velocity of a single bubble $|\mathbf{u}_\infty|$. The grid division number is 56 in both the horizontal and the vertical directions in the detection area.

It is found from Fig. 13(a) and (b) that in low Reynolds numbers bubbles rising side-by-side have high velocities to force bubbles separating each other in the horizontal direction. This

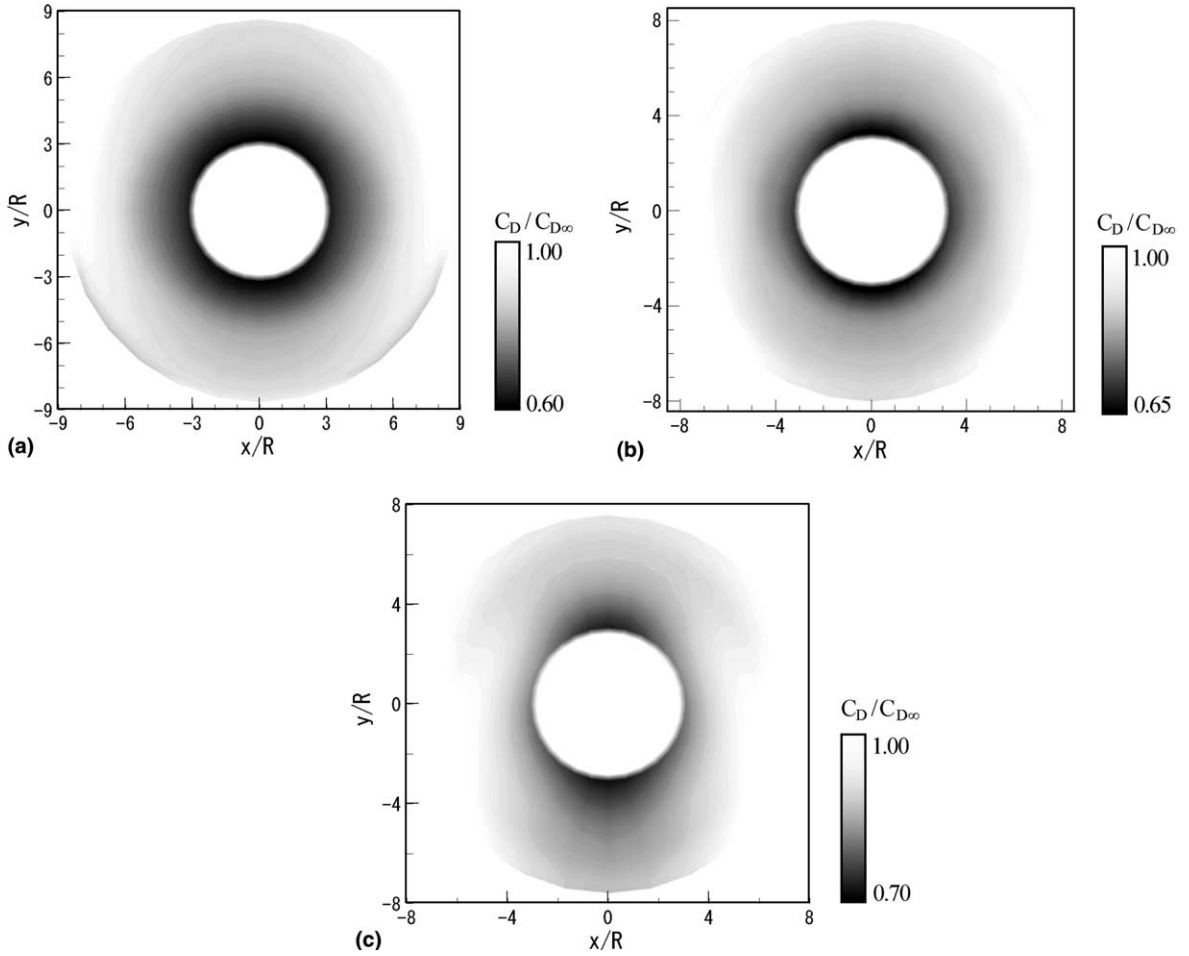

Fig. 11. Distribution of drag coefficient ratio of the nearest bubbles: (a) case b1; (b) case b2; (c) case b3.

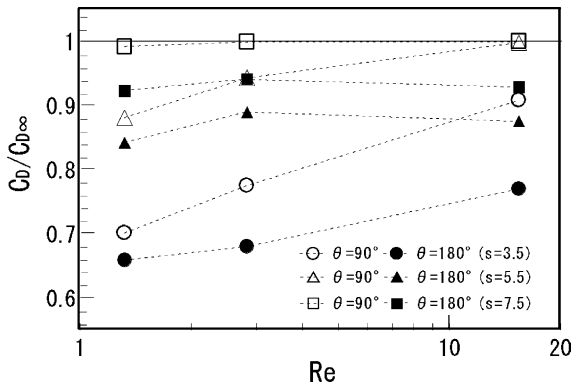

Fig. 12. Drag coefficient ratio of wall-sliding bubble rising side-by-side and in tandem.

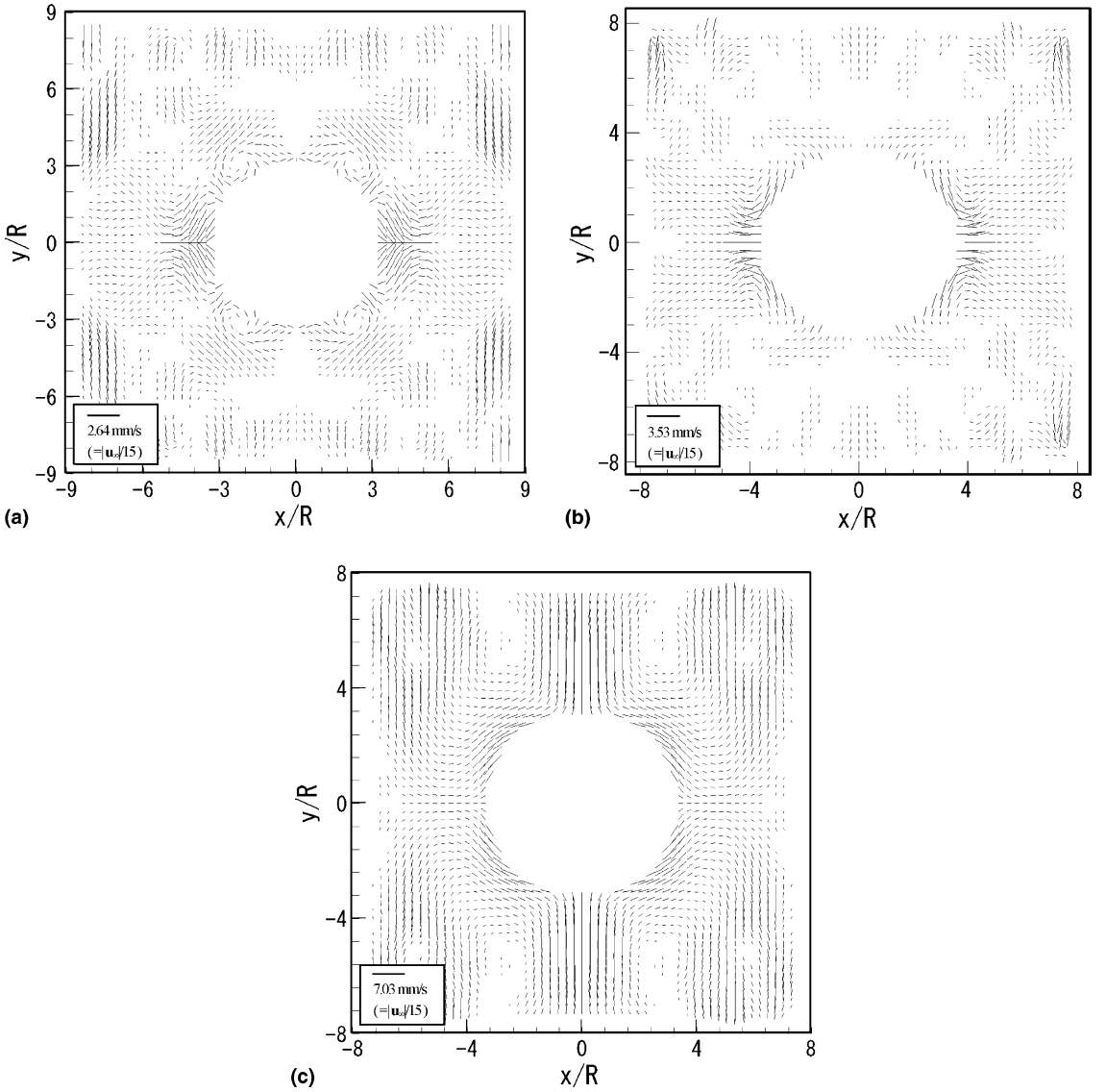

Fig. 13. Distribution of relative bubble velocity vectors: (a) case b1; (b) case b2; (c) case b3.

repulsive velocity is detected at a wider angle in the case of $Re = 1.3$ shown in Fig. 13(a). The presence of a wide repulsive velocity region might trigger the active diffusion of the bubble distribution in a low Reynolds number environment, as with micro-bubbles. To be concrete, this horizontal repulsive velocity causes the probability of the occurrence of the nearest bubble to decrease in the horizontal direction. Therefore, the frequencies shown in Fig. 8(a) and (b) increase relatively in the vertical direction.

In contrast, it is clear from Fig. 13(c) that in the high Reynolds number upper and lower bubbles to a focused bubble have a velocity that forces bubbles attracting each other. The domain in

which this velocity is detected is in the range of $|x/R| < 2$, and is limited to a narrow region in the degree of the bubble diameter. One of the reasons is the effect of the bubble wake, owing to the increase in Reynolds number. That is, the wake of the upper bubble causes the lower bubble to approach. It is also clear that bubbles rising side-by-side to a focused bubble have low velocities that force bubbles separating from each other. In the diagonal region, the above-mentioned two relative velocity vector regions are continuously connected. However, the relative velocity is quickly attenuated during the orientation changes from the vertical to the horizontal. Hence, the bubbles will stay there for a while. This is why the probability distribution reaches its peak near the horizontal side in the case of $Re = 15$. Furthermore, it is seen that bubbles in far diagonal positions have a vertical separating velocity. As the result, a relative motion appears as a circulation in the ranges of $|x/R| < 2$–4 and $|y/R| > 3$. Confirming the video images, two bubbles positioned in the diagonal arrangement surely rose with rotational displacement. This may be one of the interesting results, which are obtained by the present measurement technique based on the PTV technique.

5. Conclusions

By applying the two-dimensional particle tracking velocimetry (PTV) technique to wall-sliding bubble flows, the motion characteristics of bubble swarms sliding along a flat wall was discussed. The present study focused on the condition that the distance between the wall and the bubble interface was much shorter than the average bubble diameter. For the laminar range of Reynolds numbers up to 20, the following points have been elucidated:

1. Reducing the Reynolds number of the bubble, the difference in the drag coefficient between the single wall-sliding bubble and the single free-rising bubble becomes large. In the maximum case, the difference reaches a value of over 30% at $Re < 0.1$ and in the minimum case, a value of 15% at $Re > 15$. It is found that the variation in the drag coefficient of wall-sliding bubble depends on the kinematic viscosity of the liquid. The ratio of Reynolds number in the bubble swarm to that of a single bubble increases almost linearly with the shadow area fraction. The increasing gradient is independent of the viscosity of the liquid, and its value is approximately 6.
2. The nearest bubbles to a focused bubble in the bubble swarm at $Re < 3$ distribute frequently in the vertical direction. In contrast, the nearest bubbles at $Re = 15$ distribute frequently in the horizontal direction.
3. In the range of $Re < 3$, the rise velocities of the upper bubbles and lower bubbles to a focused bubble are almost same, while those at $Re = 15$ are different, due to the effect of the wake induced in the downstream direction. In addition, the horizontal velocity component, forcing bubbles to repulse each other, is induced when two bubbles rise side-by-side.
4. The drag coefficient is reduced by around 30% in the tandem-rising case and its ratio of the reduction is always bigger than in the side-by-side case. In addition, the reduction ratio gets large at lower Reynolds numbers. This indicates that the flow field around bubbles is altered by approaching other bubbles, especially for a viscosity-governed environment.

5. Two kinds of relative velocities between two bubbles are observed in a swarm: (1) the repulsive velocity is detected in the case of a side-by-side arrangement for any Reynolds numbers. (2) the attractive velocity is detected in a tandem arrangement for $Re = 15$. These relative motions can explain the features of the probability distribution of bubbles on the relative coordinates.

References

Brucker, C., 1998. Bubble interaction in swarms: a study of the wake structures with 3-D scanning particle image velocimetry (3-D SPIV). In: Proc. 3rd Int. Conf. Multiphase Flow'98-Lyon, CD-ROM, 1-8.

Bunner, B., Tryggvason, G., 1999. An examination of the flow induced by the motion of many buoyant bubbles. J. Visual. 2, 153–158.

Esmaeeli, A., Tryggvason, G., 1998. Direct numerical simulations of bubbly flows. Part.1. Low Reynolds number arrays. J. Fluid Mech. 377, 313–345.

Kodama, Y., Kakugawa, A., Takahashi, T., Kawashima, H., 2000. Experimental study on microbubbles and their applicability to ships for skin friction reduction. Int. J. Heat Fluid Flow 21, 582–588.

Kim, I., Elghobashi, S., Sirignano, W.A., 1993. Three-dimensional flow over spheres placed side by side. J. Fluid Mech. 246, 465–488.

Legendre, D., Magnaudet, J., 1998. Interaction between two spherical bubbles rising side by side. In: Proc. 3rd Int. Conf. Multiphase Flow'98-Lyon, CD-ROM, 1–8.

Mei, R., Klausner, J.F., Lawrence, C.J., 1994. A note on the history force on a spherical bubble at finite Reynolds number. Phys. Fluids 6, 418–420.

Moore, D.W., 1963. The boundary layer on a spherical gas bubble. J. Fluid Mech. 23, 749–766.

Nagai, N., Takeuchi, M., Kimura, T., Oka, T., 2003. Existence of optimum space between electrodes on hydrogen production by water electrolysis. Int. J. Hydrogen Energy 28, 35–41.

Nishino, K., Kasagi, N., Hirata, M., 1989. Three dimensional particle tracking velocimetry based on automatic digital image processing. ASME J. Fluid Eng. 111, 384–389.

O'Neill, M.E., 1964. A slow motion of viscous liquid caused by a slowly moving solid sphere. Mathematika 11, 67–74.

Otsu, N., 1979. A threshold selection method from gray-level histograms. IEEE Trans. Sys., Man, Cybernet. SMC-9 1, 62–66.

Prewitt, J.M.S., 1970. Object enhancement and extraction. Picture proc. psychopictorics. Academic Press, pp. 75–149.

Ruzicka, M.C., 2000. On bubbles rising in line. Int. J. Multiphase Flow 26, 1141–1181.

Sangani, A.S., Didwania, A.K., 1993. Dynamic simulations of flows of bubbly liquids at large Reynolds numbers. J. Fluid Mech. 250, 307–337.

Sangani, A.S., Zhang, D.Z., Prosperetti, A., 1991. The added mass, Basset, and viscous drag coefficients non-dilute bubbly liquids undergoing small-amplitude oscillatory motion. Phys. Fluids A 3, 2955–2970.

Serizawa, A., Kataoka, I., 1988. In: Afgan, N. (Ed.), Transient phenomena in multiphase flows. Hemispher, pp. 179–187.

Smereka, P., 1993. On the motion of bubbles in a periodic box. J. Fluid Mech. 254, 79–112.

Stewart, C.W., 1995. Bubble interaction in low viscosity liquids. Int. J. Multiphase Flow 21, 1037–1046.

Sugiyama, K., Takagi, S., Matsumoto, Y., 2001. Multi-scale analysis of bubbly flow. Comput. Meth. Appl. Mech. Eng. 101, 689–704.

Takemura, F., Takagi, S., Magnaudet, J., Matsumoto, Y., 2002. Drag and lift forces on a bubble rising near a vertical wall in a viscous liquid. J. Fluid Mech. 461, 277–300.

Taylor, T.D., Acrivos, A., 1964. On the deformation and drag of a falling viscous drop at low Reynolds number. J. Fluid Mech. 18, 466–476.

Yamamoto, F., Wada, A., Iguchi, M., Ishikawa, M., 1996. Discussion of the cross-correlation methods for PIV. J. Flow Visual. Image Process. 3, 65–78.

Yuan, H., Prosperetti, A., 1994. On the in-line motion of two spherical bubbles in a viscous fluid. J. Fluid Mech. 278, 325–349.

Zenit, R., Koch, D.L., Sangani, A.S., 2001. Measurements of the average properties of a suspension of bubbles rising in a vertical channel. J. Fluid Mech. 429, 307–342.

Zuber, N., 1964. On the dispersed two-phase flow in the laminar flow regime. Chem. Eng. Sci. 19, 897–917.